Journal of Energy Storage 92 (2024) 112169

Contents lists available at ScienceDirect

Journal of Energy Storage

journal homepage: www.elsevier.com/locate/est

Research papers

Optimizing supercapacitive performance of MXene through MOF-derived nickel ferrite nanoparticle integration

S.R. Shingte [a], V.D. Chavan [b], R.P. Dhavale [c], Deok-Kee Kim [b], Hyung-Ho Park [c], T.D. Dongale [d], P.B. Patil [a,*]

[a] Department of Physics, The New College, Shivaji University, Kolhapur, Maharashtra 416012, India
[b] Department of Electrical Engineering and Convergence Engineering for Intelligent Drone, Sejong University, Seoul, South Korea
[c] Department of Materials Science and Engineering, Yonsei University, 50 Yonsei-ro, Seodaemun-gu, Seoul 03722, South Korea
[d] Department of Nanoscience and Technology, Shivaji University, Kolhapur, Maharashtra - 416012, India

ARTICLE INFO

Keywords:
MOF
MXene
Nickel ferrite
Spacer
Asymmetric supercapacitor

ABSTRACT

To optimize the supercapacitive performance of MXene, a simple physical mixing method is used for the decoration of Metal Organic Framework (MOF)-derived rhombohedral-shaped nickel ferrite nanoparticles (NFO NPs) into the $Ti_3C_2T_x$ MXene layers. NFO NPs acted as spacers between the MXene layers resulting in a larger surface area of the nanocomposite. The loading percentage of NFO NPs was found to significantly affect the structural characteristics and thereby the supercapacitive performance of the nanocomposite. The MXene composite with 8 % NFO NPs loading (MXene/NFO-8) exhibited a specific capacitance of 660 F g^{-1} at a 1 A g^{-1}. An all-solid-state asymmetric supercapacitor (ASC) device was fabricated using the MXene/NFO-8 composite film (positive electrode) and activated carbon (negative electrode). The fabricated ASC displayed a working potential of 1.42 V, excellent cyclic durability, and an energy density of 17.36 W kg^{-1} at a power density of 718.48 Wh kg^{-1}.

1. Introduction

Due to the increasing use of fossil fuels and their harmful impact on the environment, researchers are looking for cleaner and safer sustainable energy sources [1]. Batteries and other electrochemical energy storage systems (ESS), such as supercapacitors are emerging as pivotal solutions to meet the global energy challenges by providing a dependable and efficient way to store and utilize energy [2]. Supercapacitors have several advantages over other electrochemical ESS, including the capability to charge and discharge quickly, a long lifecycle, high power density, broad operating temperature range, minimal maintenance requirements, and environmental friendliness [3]. Asymmetric supercapacitors (ASCs) consisting of positive and negative electrodes are of particular interest. This configuration enables ASCs to fully exploit the varying potential ranges of their two electrodes, thereby allowing the ASC to achieve maximum operational voltage. Consequently, this enhances the overall power density of the device, making it a promising technology for high-performance energy-storage solutions [4]. Nonetheless, supercapacitors consistently encounter the obstacle of a notably lower energy density than batteries. This limitation significantly restricts their viability as efficient energy storage solutions [5]. Various approaches and methods have been investigated for enhancing the energy density of supercapacitors. These include the optimization of electrolytes [6], adjustment of operating voltages [7], and innovation in electrode materials [8]. In general, the effectiveness of supercapacitors mostly depends on the structure and composition of electrode materials. Therefore, it is crucial to prioritize research and innovation in the development of novel electrode materials.

Recently, significant attention has been paid to the utilization of a fascinating class of 2D materials, referred to as MXene, specifically focusing on $Ti_3C_2T_x$, for the supercapacitors [9]. $Ti_3C_2T_x$ (T_x = surface functional groups) is typically synthesized using hydrofluoric acid solution (HF) to remove the Al atomic layers from Ti_3AlC_2. This etching method selectively preserves Ti and C layers and induces some specific T_x (such as O, OH, and F) on the exposed Ti surfaces of the Ti_3C_2 layers [10]. $Ti_3C_2T_x$, exhibits remarkable properties, for instance, strong electrical conductivity within the range of 6000–8000 S cm^{-1}, abundance surface functional groups, adjustable interlayer spacing, and

* Corresponding author.
E-mail address: prashantphy@gmail.com (P.B. Patil).

https://doi.org/10.1016/j.est.2024.112169
Received 21 February 2024; Received in revised form 24 April 2024; Accepted 17 May 2024

facile ion accessibility in aqueous electrolytes [11]. These distinctive characteristics make MXene materials exceptionally promising for enhancing electrochemical performance [12]. Unfortunately, owing to the robust van der Waals forces and electrostatic interactions between the layers of MXene materials, they tend to undergo irreversible agglomeration and stacking. This phenomenon significantly impedes the efficient transmission of ions within the MXene structure, thereby diminishing its overall energy storage capabilities [13]. Numerous strategies have been established to tackle this challenge, including the fabrication of porous architectures [14], the construction of three-dimensional macroporous frameworks [15], and the incorporation of interlayer spacers [16]. The use of metal-organic frameworks (MOFs) as interlayer spacers between MXene layers presents a convincing approach to prevent undesirable restacking of MXene layers [15,16]. MOFs provide a large surface area per unit volume due to their porous nature. This unique feature is attributed to the open channels and nanoscale cavities within MOFs, which accelerate the flow of electrons, a key attribute for energy storage applications [17]. Moreover, MOFs have abundant pseudocapacitive redox centers and are stable in both acidic and basic environments and hence well-suited for supercapacitors which often operate under harsh conditions [18,19]. Shasha Zheng et al, synthesized the Ni MOF-MXene composite to deal with the problem of poor conductivity of Ni-MOF, and the resulting MXene@Ni-MOF demonstrated a specific capacitance (C_{SP}) of 979 F g^{-1} at 0.5 A g^{-1} [20]. Jiaheng Wang et al, constructed MXene-Ni-Co@NiCo-MOF/Ni foam hybrid supercapacitor which achieved the specific capacity of 855.0C g^{-1} at 1 A g^{-1} [21].

However, pristine MOFs exhibit low conductivity, which hinders their utility in supercapacitors. Therefore, instead of pristine MOFs, the use of MOFs-derived nanomaterials by annealing MOFs as sacrificial templates can be used as novel electrode materials [22,23]. It not only maintains the porous structure found in MOFs but also demonstrates remarkable electrical conductivity [24]. Owing to the enhanced redox capabilities exhibited by various nickel states, MOF-derived nickel ferrite nanoparticles (NFO NPs) have been discovered as a promising material for supercapacitor electrodes [25]. Considering the remarkable electrical conductivity of MXene [26,27] and the notable redox activity of MOF-derived materials, it is interesting to explore efficient preparation methods and application of conductive matrices integrated with MOF-based composites in supercapacitors.

In this study, MOF-derived rhombohedral-shaped NFO NPs were decorated into the $Ti_3C_2T_x$ MXene layers via a physical mixing method. These NFO NPs act as spacers between the MXene layers. This spacing enlargement promotes an efficient charge transfer process. An investigation was carried out to examine the effects of the NFO loading percentage on both the structural and supercapacitive properties of the composites. Electrochemical measurements demonstrated that the MXene composite with 8 percentage NFO NP loading (MXene/NFO-8) displays a C_{SP} of 660 F g^{-1} when subjected to a current density of 1 A g^{-1}. An all-solid-state asymmetric supercapacitor (ASC) device was developed where composite film acts as the positive electrode while activated carbon serves as the negative electrode. The fabricated ASC showed a working potential of 1.42 V, exceptional cyclic durability, and remarkable power density (P.D.) of 718.48 W kg^{-1}, coupled with energy density (E.D.) of 17.36 Wh kg^{-1}.

2. Experimental methods

Chemicals and materials, and characterizations sections are provided in the supplementary material file.

2.1. Preparation of MOF-derived nickel ferrite (NFO)

The MOF-derived NFO was prepared by the solvothermal method. Initially, Ni $(NO_3)_2{\cdot}6H_2O$ (3.3 mM) and $FeCl_3{\cdot}6H_2O$ (6.7 mM) were dissolved in 10 mL volume of *N*, *N*-Dimethylformamide (DMF). Subsequently, a separate solution comprising terephthalic acid (9.9 mM) dissolved in 10 mL of DMF was introduced into the aforementioned mixture while maintaining continuous stirring for 1 h to ensure a uniform solution. The NaOH solution (400 mM) was gradually added to the mixture to obtain the precipitate and stirred for another 15 min at room temperature (RT). The resulting precipitate was carefully put into a Teflon-coated autoclave and heated at 100 °C for a duration of 15 h. The sample was then rinsed thrice with DMF and double-distilled water (DDW) and was dried for 2 h at 60 °C. The final step involved the annealing of the prepared sample, initially at 100 °C for 2 h and then at 500 °C for 6 h. This annealed product was designated as NFO.

2.2. Preparation of $Ti_3C_2T_x$ MXene

The commercially available Ti_3AlC_2 powder (MAX phase) (1 g) was added slowly into 20 mL hydrofluoric acid solution (40 %) and stirred for 12 h at RT. The resulting etched product was washed using DDW and ethanol until around 7 pH was reached [28]. The obtained dark sediment was dried for 24 h in a vacuum oven.

2.3. Preparation of MXene/NFO-x

In a typical synthesis of MXene/NFO- x composite, x % of NFO relative to MXene (x = 4 %, 8 %, 16 %, and 24 %) was carefully dispersed in 20 mL of DDW using ultrasonication for 30 min. The MXene (20 mg) was mixed in NFO dispersion and stirred for 15 min. To ensure uniform dispersion of MXene/NFO, it was further ultrasonicated for 30 min. All the processes were carried out at RT. Then the MXene/NFO product was subjected to centrifugation and allowed to dry in a vacuum desiccator. The formation mechanism of MXene/NFO composite material is explained in the supplementary material file.

2.4. Fabrication of working electrode

To fabricate the working electrode, the following procedure was followed: a uniform mixture of active materials (NFO, or MXene, or MXene/NFO-*x*), activated carbon (AC), and polyvinylidene fluoride (PVDF) (in a mass ratio of 8:1:1) was carefully blended in N-Methyl-2-pyrrolidone (NMP) solvent. The obtained slurry was brush-coated onto a porous nickel foam (1 * 1 cm^2), ensuring a mass loading of 2 to 5 mg. The coated electrode was subsequently dried at 50 °C for 12 h to effectively remove any residual solvent.

An ASC device was fabricated using MXene/NFO-8 composite as a positive electrode whereas AC was the negative electrode. The negative AC electrode was developed using a slurry of AC and PVDF in a 9:1 ratio. The electrolyte utilized in the experiment comprised a gel formed from a combination of polyvinyl alcohol (PVA) and potassium hydroxide (KOH). To obtain this PVA/KOH gel electrolyte, PVA (1 g) was dissolved in 5 mL DDW. This mixture was continually stirred while heated to 80 °C for 5 h. Subsequently, 5 mL of KOH (1 M) solution was added and continuously stirred until a consistent gel texture was achieved. An ASC device was constructed by placing the Whatman Grade 41 filter paper wetted with the gel electrolyte between the MXene/NFO-8 electrode and the AC electrode.

2.5. Electrochemical measurements in a three-electrode system

The electrochemical characteristics of NFO, MXene, and MXene/NFO electrodes were investigated using a three-electrode setup at RT using the Metrohm Autolab PGSTAT204 electrochemical workstation. In this setup, the auxiliary electrode was a platinum wire, while the reference electrode was Ag/AgCl. An aqueous solution of KOH (2 M) with a pH 14 was used as an electrolyte. To assess the electrochemical performance of the synthesized nanomaterials, various measurement techniques were employed. These techniques include cyclic voltammetry (CV), galvanostatic charge-discharge (GCD), and electrochemical

impedance spectroscopy (EIS).

3. Results and discussion

The X-ray diffraction (XRD) investigation (Fig. 1) of the as-synthesized NFO, delaminated flakes of MXene, and their composites (MXene/NFO-*x*) was conducted. The standard diffraction data corresponding to MXene (JCPDS file no. 00-032-1383) and NFO (JCPDS. file no 00-010-0325) are shown in orange and cyan colour in Fig. 1. In the XRD pattern of MXene, a characteristic peak of the MAX phase at 39° corresponding to (104) planes is absent. This absence strongly indicates that the 'Al' component of Ti_3AlC_2 has been successfully removed, resulting in the MXene sheets [29]. A prominent (002) peak at 8.3° confirms the formation of MXene. Furthermore, relatively weaker peaks at 18.22°, 27.48°, 41.76°, and 60.74° can be ascribed to the (004), (008), (200), and (220) planes of the exfoliated Ti_3C_2 layers, respectively. Moreover, the presence of $Ti_3C_2F_x$ was evident from the distinct peaks at 2θ values 8.3° and 18.22°, indicating the attachment of —F groups on the MXene surface [30]. The peak at 27.48° corresponds to $Ti_3C_2(OH)_2$, indicating that the MXene surfaces have been terminated with -OH groups. The presence of such negative groups is useful for its composite with NFO. The XRD pattern of NFO reveals distinct peaks at 18.4°, 30.1°, 35.7°, 43.3°, 53.8°, 57.3°, and 62.91°. The indexing of these peaks corresponds to the (111), (220), (311), (400), (422), (511), and (440) planes, as specified in JCPDS file No. 00–010–0325 and has been correlated with the cubic spinel structure of $NiFe_2O_4$. In the XRD patterns for the MXene/NFO-*x*, the crystal planes associated with both the MXene and NFO were observed. This observation is indicative of the successful integration of MXene and NFO in the composite. The (002) peak of associated with the MXene in the composite undergoes a shift from 8.3° to 8.6° when compared to pure MXene. This shift is attributed to the incorporation of NFO into the composite, signifying the interactions between MXene and NFO. Furthermore, as the NFO content in the MXene/NFO composites increases, a gradual enhancement in the NFO peak intensities was observed.

The morphological characteristics and microstructures of MXene, NFO, and MXene/NFO-*x* composite materials were observed using field emission scanning electron microscopy (FESEM), and the findings are depicted in Fig. 2. The FESEM image of MXene shown in Fig. 2A reveals the presence of well-organized layers of MXene nanosheets featuring

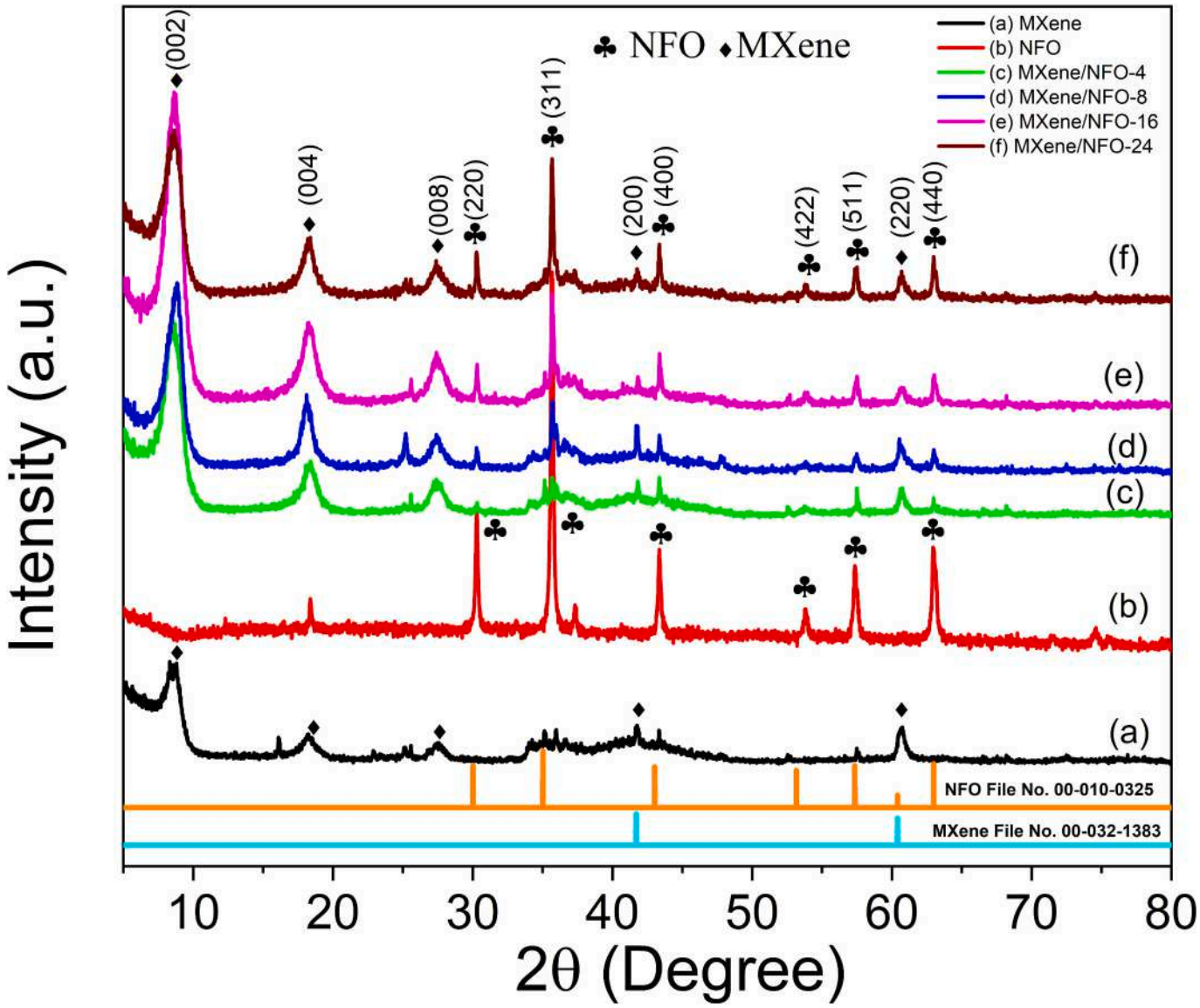

Fig. 1. XRD patterns of (a) MXene, (b) NFO, (c) MXene/NFO-4 (d) MXene/NFO-8, (e) MXene/NFO-16, and (f) MXene/NFO-24. (The standard diffraction data corresponding to MXene (JCPDS file no. 00-032-1383) and NFO (JCPDS. file no 00-010-0325) shown in orange and cyan colour). (For interpretation of the references to colour in this figure legend, the reader is referred to the web version of this article.)

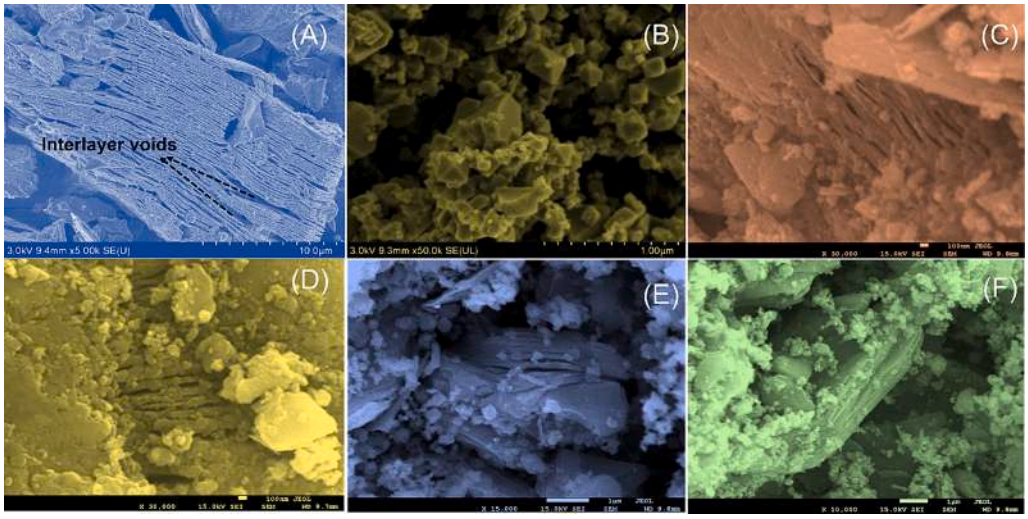

Fig. 2. FESEM images of (A) MXene, (B) NFO, (C) MXene/NFO-4, (*D*) MXene/NFO-8, (E) MXene/NFO-16, and (F) MXene/NFO-24.

interlayer voids. An interesting accordion-like structure emerged as a result of the exfoliation of MXene basal planes following the removal of 'Al' atoms. The FESEM observations of NFO NPs, provided in Fig. 2B demonstrate their rhombus-like structure. The FESEM images of MXene/NFO-*x* composites, as depicted in Fig. 2(C—F), illustrate the integration of NFO NPs onto the MXene layers' surface as well as within the gaps between these layers. In MXene/NFO composite, MXenes possess negatively charged surfaces due to terminal functional groups like hydroxyl and fluorine. NFO, on the other hand, can have positively charged metal centers as can be observed from the schematic representation of MXene/NFO material (Fig. S1 of supplementary file). This causes electrostatic interaction between the MXene and NFO components which facilitates interfacial contact during mixing [31]. Also, the weak van der Waals forces can arise between the MXene and NFO particles due to their proximity during mixing. These forces contribute to the physical adhesion between the two materials in the MXene/NFO composite. Furthermore, during the mixing process, the sheet-like morphology of MXenes can entangle with the porous structure of the NFO [32]. This physical interlocking can also strengthen the interaction between the two components of the MXene/NFO composite. With an increase in NFO content from 4 % to 24 %, the aggregation of NFO particles can also be seen to be increased.

Transmission electron microscopy (TEM) was utilized to analyze the microstructures of MXene, NFO, and MXene/NFO-8 composite (Fig. 3). As can be seen in Fig. 3A, MXene is nearly transparent when viewed under TEM as it is composed of very thin nanosheets. These two-dimensional MXene nanosheets play a crucial role in facilitating electron transport. The TEM micrograph of NFO (Fig. 3B) displays well-defined and randomly distributed rhombus-shaped, smooth-surfaced nanoplates. From the TEM micrograph of MXene/NFO-8 (Fig. 3C), it can be observed that the rhombus-shaped NFO nanoplates are wrapped by the two-dimensional MXene layers, creating a uniform 2D—3D hybrid structure. This formation is vital as it provides sufficient pseudocapacitive active sites and enhances diffusion channels for efficient redox conversion. The selected area electron diffraction (SAED) pattern of MXene/NFO (Fig. 3D) reveals characteristic rings consistent with a polynanocrystalline structure. Within this SAED pattern, the apparent crystal plane (311) corresponds to NFO. On the other hand, planes (220), (222), and (511) correspond to the MXene. High-resolution TEM image of MXene/NFO-8 and the corresponding inverse Fast-Fourier Transform (FFT) analysis is demonstrated in Fig. 3E. The lattice fringe spacing of a cubic crystal of MXene was determined to be 0.964 Å and 1.024 Å, indicating the presence of (420) planes within the structure (JCPDS. No. 00-032-1383) and (800) planes of cubic crystal of NFO

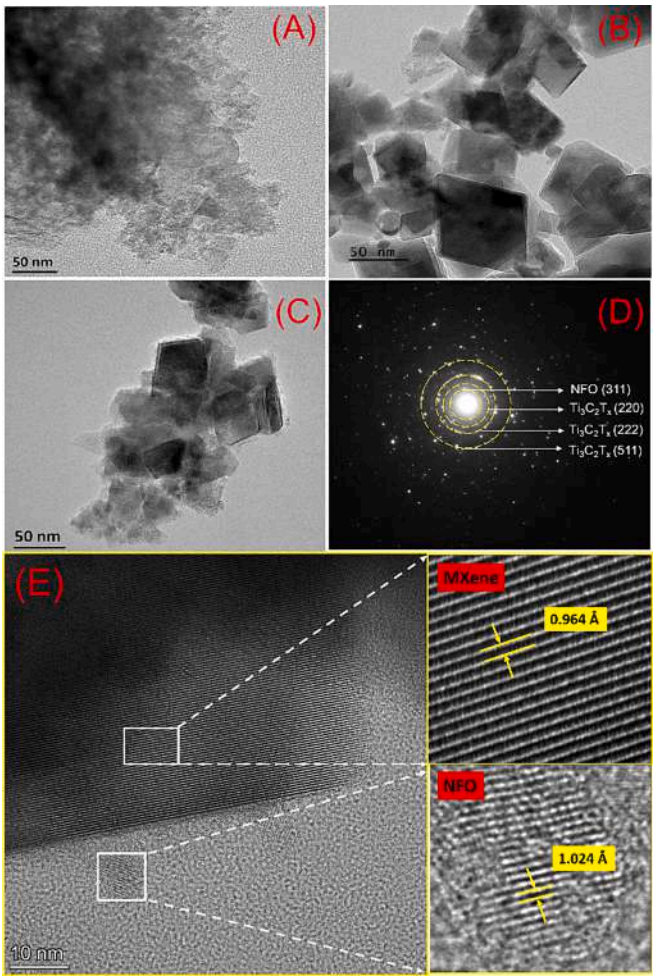

Fig. 3. TEM images of (A) MXene, (B) NFO, and (C) MXene/NFO-8. (D) Selected area electron diffraction (SAED) pattern of MXene/NFO-8, and (E) HRTEM image of MXene/NFO-8 composite with the measured d-spacing of MXene and NFO.

(JCPDS No. 00–010–0325), respectively. This confirms the presence of NFO NPs and MXene nanosheets in the composite.

Fig. 4 presents a high-angle annular dark-field scanning transmission

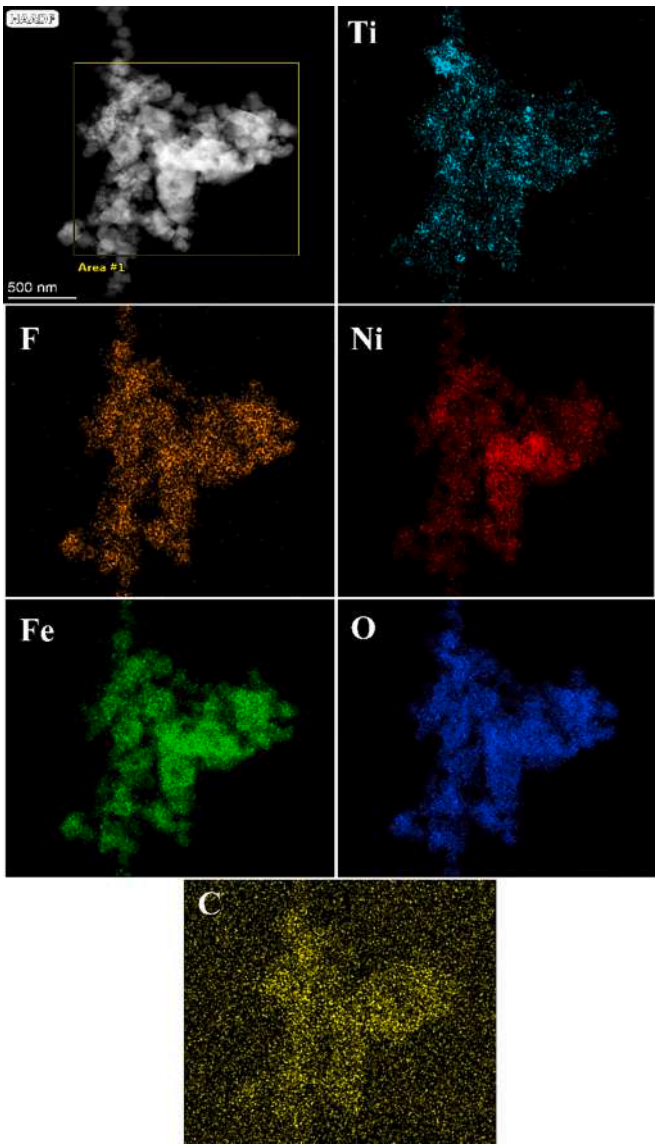

Fig. 4. HAADF STEM image and related energy dispersive X-ray spectroscopy (EDS) elemental mapping of MXene/NFO-8.

electron microscopic (HAADF STEM) image of MXene/NFO-8 along with the Energy dispersive X-ray spectroscopy (EDS) elemental mapping highlighting various constituent elements. The elemental mapping depicts the spatial distribution of Ti, C, F, O, Ni, and Fe elements in MXene/NFO-8. The uniform distribution of Fe and Ni in the nanocomposites demonstrates the uniform integration of NFO NPs with MXene sheets. Moreover, the presence of O and F elements collectively validate the presence of surface terminal groups like -F and -OH on the MXene material.

To probe the chemical makeup and surface electronic characteristics of the MXene/NFO-8 composite, X-ray photoelectron spectroscopy (XPS) was employed (Fig. 5). The XPS survey spectrum (Fig. 5A) indicates the presence of C, Ti, F, O, Fe, and Ni within the composite. Among these elements, Ti, F, and C are attributed to the $Ti_3C_2F_x$ component while Fe, Ni, and O are associated with the NFO component. The analysis of the high-resolution XPS spectrum of Ti 2p (Fig. 5B) reveals distinct peaks corresponding to various chemical states. These peaks can be attributed to C-Ti-F_x (459.8 eV), Ti^{2+} (456.2 eV), Ti^{3+} (465.6 eV), and TiO_2 (463.5 eV), indicating a slight oxidation process occurring within the MXene sheets [33]. Three peaks could be identified by deconvolution of the O 1 s XPS spectra of MXene/NFO-8 (Fig. 5C) at 529.3, 530.8, and 532.7 eV, which are ascribed to Ni—O, surface active oxygen, and C-Ti-$(OH)_x$, respectively. These findings from the Ti 2p and O 1 s spectra collectively suggest the partial oxidation of $Ti_3C_2T_x$ MXene to TiO_2 due to the increased defects and a larger proportion of exposed nanosheet surfaces. In the XPS spectrum of Fe depicted in (Fig. 5D), two main peaks appear at ~711.5 and ~725 eV. These specific peaks are indicative of the spin-orbit doublet associated with Fe 2p, specifically denoting Fe $2p_{3/2}$ and Fe $2p_{1/2}$, respectively [25]. The broader and more intense Fe $2p_{3/2}$ peak has been deconvoluted into two subpeaks, 711.3 eV (attributed to Fe^{3+} in an octahedral (Oh) coordination environment) and 713.5 eV (indicative of Fe^{2+}). The Fe $2p_{1/2}$ peak observed at 724.3 eV is typically linked to Fe^{3+} (Oh) while the peak at 726.5 eV is commonly linked with Fe^{3+} (Td). The Ni 2p spectra (Fig. 5E) may be generally classified into two edges: Ni $2p_{1/2}$ (870–876 eV) and Ni $2p_{3/2}$ (851–860 eV) edges, which are separated by spin-orbit coupling [34]. The principal peak at Ni $2p_{3/2}$ was resolved into distinct components at 855.9 eV and 854.06 eV, denoting the presence of Ni^{2+} in tetrahedral (Td) and octahedral (Oh) coordination environments, respectively. Alongside these primary peaks, there is an additional satellite peak having a binding energy of 861.9 eV. The spectral lines associated with Ni $2p_{3/2}$ were observed at 864.6 eV corresponding to the satellite peak originating from NiO. Furthermore, Ni $2p_{1/2}$ peak is also deconvoluted into 872.6 eV (Ni^{2+} Oh) and 873.7 eV (Ni^{2+} Td). These peaks indicate the presence of Ni^{2+} state [25]. High-resolution C1s region XPS spectrum (Fig. 5F) of the MXene/NFO-8 composite revealed three main peaks occurring at 289.4 eV, 285.5 eV, and 282.2 eV, due to O-C=O/C-F, C—O and Ti—C, respectively [35].

Fig. 6 illustrates the N_2 adsorption-desorption isotherms observed for MXene, NFO, and MXene/NFO-8 at a temperature of 77.35 K. Additionally, the inset graphically represents the Barrett-Joyner-Halenda (BJH) pore size distribution curve associated with the data. The presence of a mesoporous structure in all samples is confirmed by the characteristic type-IV isotherm curve with an H_3 hysteresis loop [36]. The isotherm of N_2 adsorption-desorption and BJH curves of MXene/NFO-4, MXene/NFO-16, and MXene/NFO-24 are shown in Fig. S2. The BET surface areas (S_{BET}) for MXene, NFO, MXene/NFO-4, MXene/NFO-8, MXene/NFO-16, and MXene/NFO-24 are found to be 55.30, 49.49, 74.83, 81.92, 80.50, and 60.81 $m^2\,g^{-1}$, respectively. The MXene/NFO-*x* composite samples demonstrate a noteworthy improvement in S_{BET} compared to its constituent materials. This enhancement can be attributed to the combined effects of mesoporous interlayer voids within the MXene sheets, an expanded interlayer spacing between the MXene sheets, and interconnected pores originating from the MOF-derived NFO material. The S_{BET} of MXene showed a progressive rise with the incorporation of NFO until reaching a certain threshold for MXene/NFO-8. This increase can be attributed to the intercalation of NFO NPs, which exposes the basal plane of the MXene material. However, as the NFO content was further increased beyond 8 %, a decline in S_{BET} was observed. This decline was primarily caused by the aggregation of NFO NPs, which filled the pores within the MXene matrix, leading to a reduction in the available surface area [37]. Increased surface area can potentially enhance electrochemical performance by offering a greater number of active sites. The insets of Fig. 6 and Fig. S2 provide insights into the pore size (d_{pores}) distribution of MXene, NFO, and MXene/NFO-*x*, primarily falling within the 2 to 8 nm range, confirming their mesoporous nature. The S_{BET}, pore volume (V_{pores}), and d_{pores} of each sample are provided in Table S1.

3.1. Electrochemical measurements

CV measurements for all the samples were carried out to understand the dynamics of the charge transfer process and the mechanisms involved in charge storage in the supercapacitor. These measurements were conducted out in 2 M KOH within a potential range of 0 to 0.6 V. Fig. 7A displays the CV curves for MXene, NFO, and MXene/NFO-8 composite and Fig. S3(A) displays comparative CV curves for MXene/

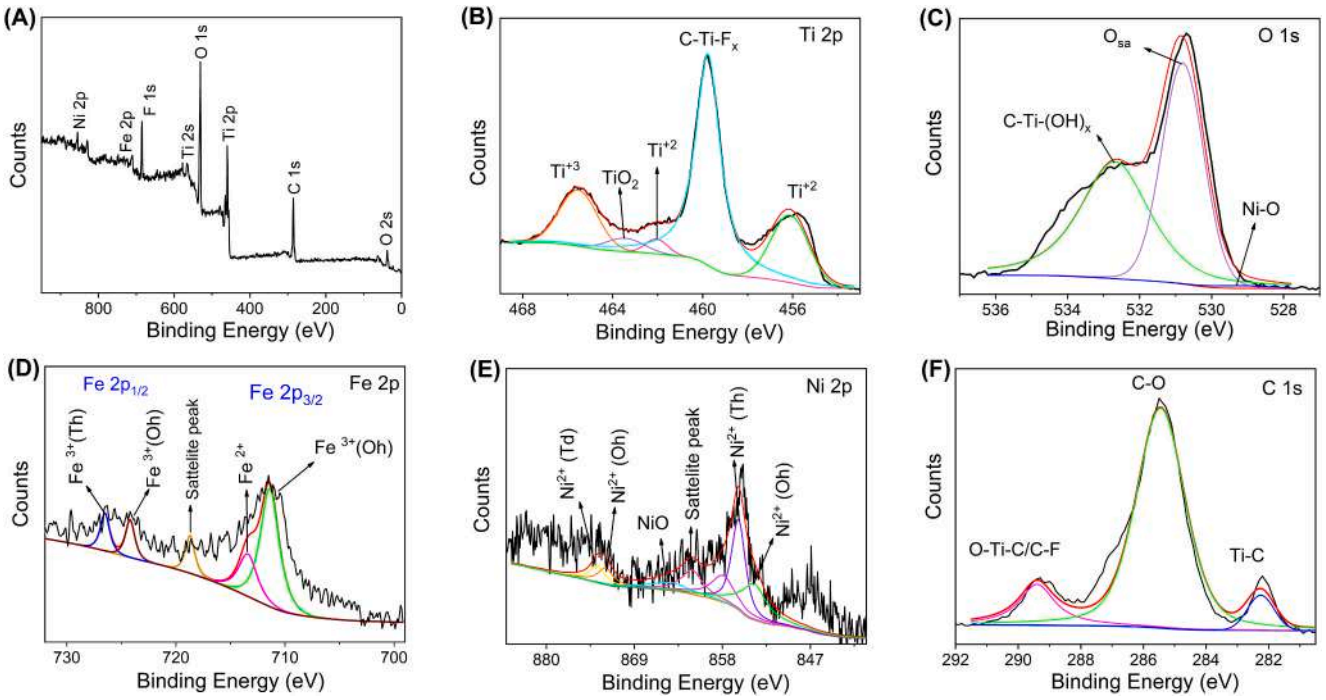

Fig. 5. (A) Full XPS survey spectrum of MXene/NFO-8. Deconvulated XPS spectra of (B) Ti 2p, (C) O 1s, (C) Fe 2p, (E) Ni 2p, and (F) C1s.

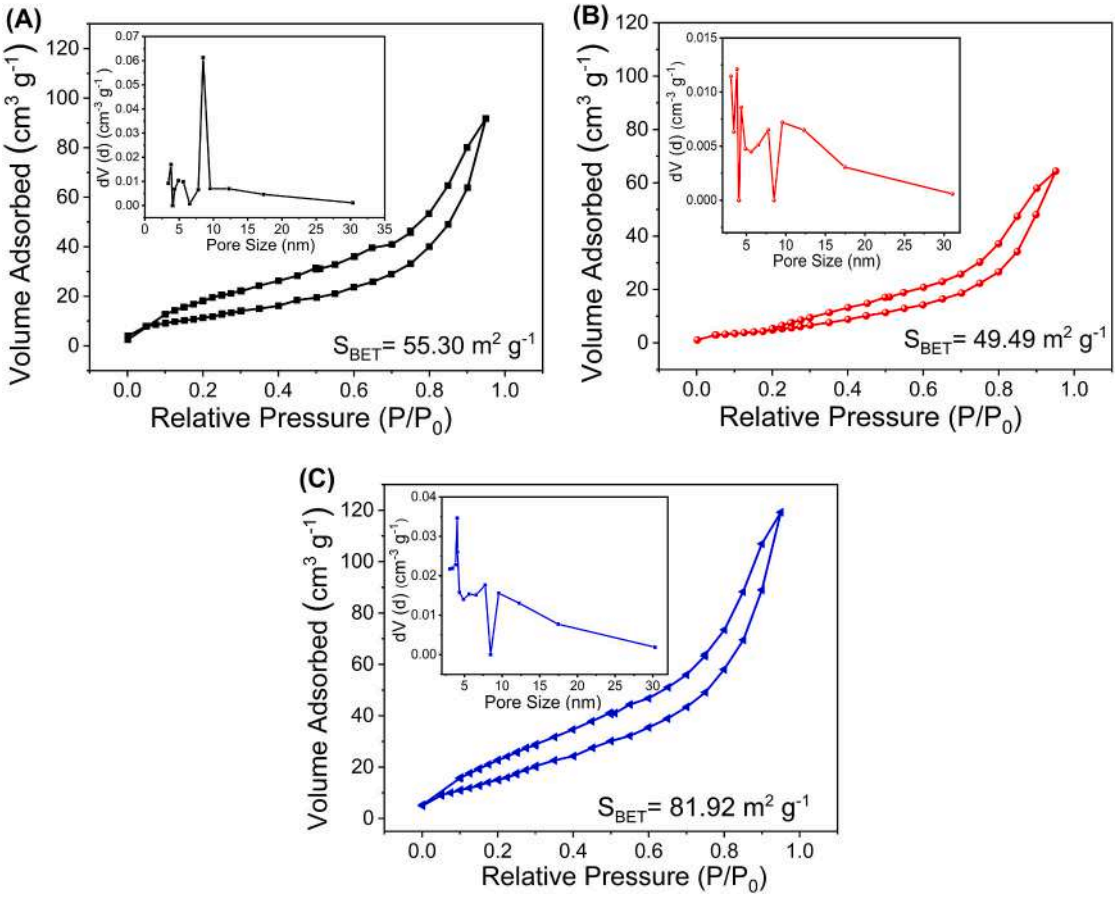

Fig. 6. N_2 adsorption-desorption isotherms of (A) MXene, (B) NFO, and (C) MXene/NFO-8. The inset displays the pore size distribution of the corresponding material.

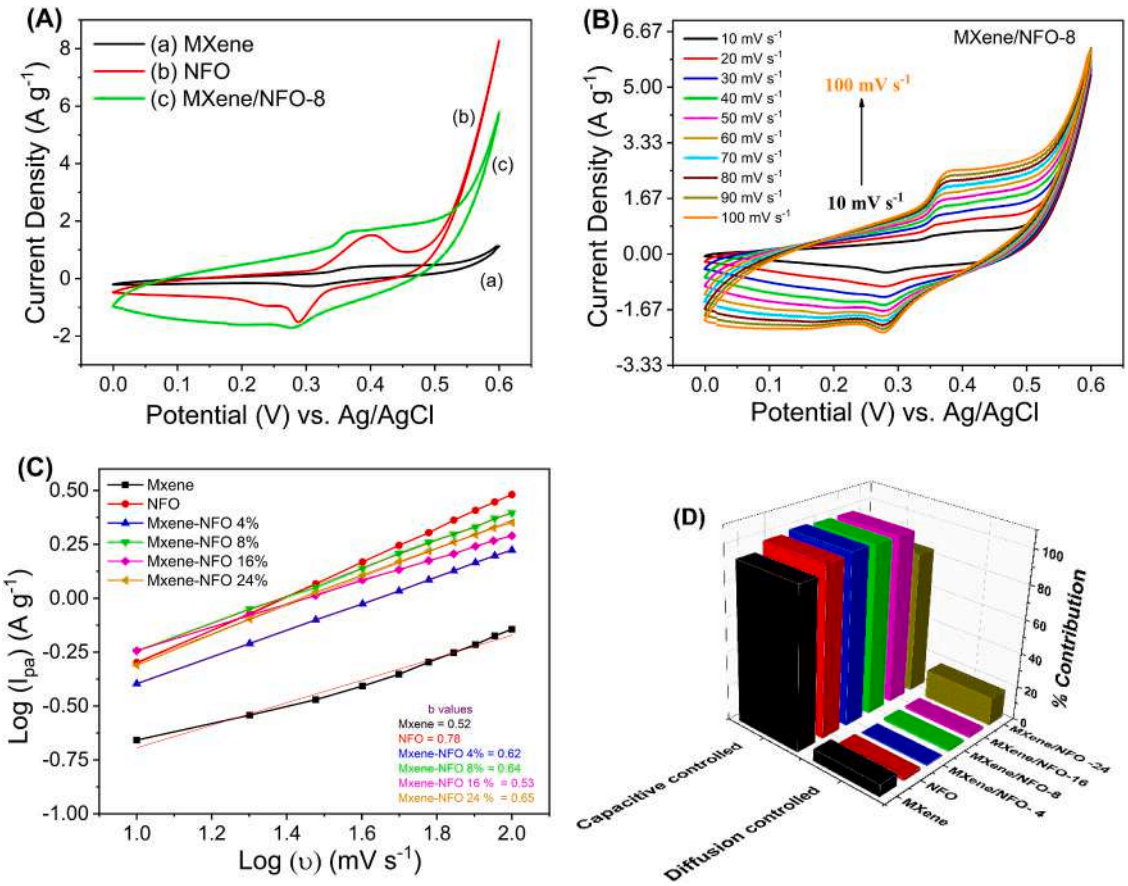

Fig. 7. (A) CV profiles of MXene, NFO, and MXene/NFO-8 at a 50 mV s^{-1}. (B) CV curves of MXene/NFO-8 at 10 to 100 mV s^{-1} scan rate. (C) The plot of Log (I_{pa}) vs. Log (υ) for calculation of b-value for MXene, NFO, and MXene/NFO-*x* samples. (D) Surface-induced and diffusion-controlled capacitance contribution of various electrode materials at 10 mV s^{-1} based on Trasatti analysis.

NFO-*x* electrodes. The CV profiles of each sample exhibited distinct redox peaks, indicative of their pseudocapacitive nature. The observed distinct pair of redox peaks for MXene/NFO-*x* resembled the transition of Ni^{2+}/Ni^{3+} and Fe^{2+}/Fe^{3+} as per the following equations [29].

$$NiFe_2O_4 + H_2O + OH^- \leftrightarrow 2FeOOH + NiOOH + e^- \quad (1)$$

$$NiOOH + OH^- \leftrightarrow NiO_2 + H_2O + e^- \quad (2)$$

$$FeOOH + H_2O \leftrightarrow Fe(OH)_3 \leftrightarrow (FeO_4)^{-2} + 3e^- \quad (3)$$

The redox peaks of Ni^{2+}/Ni^{3+} and Fe^{2+}/Fe^{3+} overlap due to their closely matched redox potentials. During charging, Ni^{2+} ions are oxidized to Ni^{3+} ions, while Fe^{3+} ions are reduced to Fe^{2+} ions. This process involves the reversible insertion and extraction of ions (such as K^+ or OH^-) into the crystal lattice of nickel ferrite. It causes the transfer of electrons between the electrode material and the electrolyte, contributing to the pseudocapacitive behavior. MXene possesses both high electronic conductivity and fast ion diffusivity and hence promising platform for intercalation pseudocapacitance. The interlayer space between MXene layers contributes to fast ion intercalation as well as high-density charge storage. In MXene, the surface redox reactions attributed to the ion-intercalation and deintercalation process can be elucidated through the expression [38],

$$Ti_3C_2(OH) + K^+ + e^- \leftrightarrow KTi_3C_2(OH) \quad (4)$$

This process of K^+ ion intercalation into $Ti_3C_2T_x$ MXene results in intercalation pseudocapacitance. The MXene/NFO-*x* composites show improved redox peak current and larger CV areas compared to that of pristine MXene and NFO. This improvement demonstrates the synergistic benefits of using both MXene and NFO together. The expansion in CV areas and enhanced peak current can be ascribed to the expanded surface area offered by the NFO and improved conductivity facilitated by the presence of MXene in the composite [29]. The energy storage mechanism of MXene/NFO in KOH electrolyte is a combination of pseudocapacitive behavior arising from redox reactions of metal cations of NFO and intercalation pseudocapacitance from $Ti_3C_2T_x$. Overall MXene/NFO composite exhibits enhanced conductivity, complex surface chemistry, and a multi-layered architecture, facilitating rapid electron and ion mobility, thereby boosting electrochemical performance.

Furthermore, Fig. S3(A) reveals that, as the percentage of NFO loading increases, there is an initial rise in both the current responses and the integrated CV area, followed by a subsequent decline. This phenomenon can be explained by the creation of an "electron-ion highway" formed by the synergy between MXene and NFO. This highway significantly enhances the electron transfer rate and active site utilization of MXene, leading to improved electrochemical performance. However, an excessive amount of NFO in the composite could offset the capacitance of MXene. The optimal balance between these factors was achieved at a loading of 8 % NFO in the MXene/NFO composite film, resulting in the highest current response. Furthermore, to get more information about the charge transfer characteristics of the MXene, NFO, and MXene/NFO-8, CVs were run at varying scan rates ranging from 10 to 100 mV s^{-1}. The CV profiles for MXene/NFO-8 at different scan rates are illustrated in Fig. 7B, while those for MXene and NFO are presented in Fig. S3(B) and Fig. S3(C), respectively. Increasing the scan rate leads to a proportional rise in current accompanied by well-defined peaks is observed.

The total charge stored in the electrode is a conjugation of diffusion-controlled faradaic and surface-induced capacitive contributions [39]. These contributions were evaluated by analyzing the logarithmic correlation between the peak current (I) and scan rate (υ) at a particular potential (Fig. 7C), as elucidated by the power law equation [40].

$$I = av^b \tag{5}$$

wherein a and b are variables; b is the slope determined through the plot log I_{pa} versus log υ. The value of 'b' gives insights into the nature of charge storage kinetics. Specifically, when b = 1, suggests surface-controlled capacitive charging mechanisms while b = 0.5 was linked with diffusion-controlled processes. The 'b' value within a range of 0.5 to 1.0, signifies a transitional zone where battery-type materials intersect with pseudocapacitive materials [41]. The determined b-values for MXene, NFO, MXene/NFO-4, MXene/NFO-8, MXene/NFO-16, and MXene/NFO-24 were found to be 0.52, 0.78, 0.62, 0.64, 0.53, and 0.65, respectively. These findings suggest that the mechanism underlying charge storage in these materials encompasses of surface-induced capacitive process as well as a diffusion-controlled process, which is associated with bulk effects [42]. To calculate the charge storage contributions to the overall capacitance, the Trasatti analysis was employed. Based on the Cottrell equation, the surface-controlled capacitance contribution (referred to as Co: outer) and the diffusion-controlled capacitance contribution (referred to as Ci: inner) were calculated by using the equations [43],

$$C = k_2 \upsilon^{-\frac{1}{2}} + C_o v \tag{6}$$

$$C = k_1 \upsilon^{\frac{1}{2}} + \frac{1}{C_T} \tag{7}$$

$$C_i = C_T - C_o \tag{8}$$

where C = gravimetric capacitance, C_T = total C_{SP}, C_o = outer surface contribution, and C_i = inner diffusion-controlled contribution. K_1 and K_2 are the slope and intercept, respectively. The total capacitance contributions from C_o and C_i were determined using the plots of C vs $\upsilon^{-1/2}$ (Fig. S4(A)) and 1/C vs $\upsilon^{1/2}$ (Fig. S4(B)). The quantification of the charge stored by capacitive and diffusion mechanisms at 10 mV s^{-1} for all six electrodes is shown in Fig. 7D. MXene/NFO-*x* exhibited a higher surface-controlled capacitive contribution than pristine MXene, indicating a short distance of ion diffusion and efficient electronic transmission within the MXene/NFO-*x* composites [44].

The GCD measurements were conducted to assess various electrochemical performance metrics, including capacitance, energy, and power density (Fig. 8). Fig. 8A illustrates the GCD curves of MXene, NFO, and MXene/NFO-8 at 1 A g^{-1} current density. The GCD curves of MXene/NFO-*x* composites are displayed in Fig. S5(A). All these GCD profiles exhibit nonlinearity and asymmetry indicative of pseudocapacitive behavior. The C_{SP} of all the electrode materials was computed utilizing equation [45],

$$C_{SP} = \frac{I\Delta t}{m\Delta v} \tag{9}$$

where I, Δt, and Δυ denote the discharge current, discharge duration, and voltage window, respectively. The amount of the active material is denoted as 'm'.

MXene, NFO, MXene/NFO-4, MXene/NFO-8, MXene/NFO-16, and MXene/NFO-24 exhibited the C_{SP} of 486, 540, 604, 660, 600, and 548 F g^{-1}, respectively at 1 A g^{-1}. The MXene/NFO-8 composite has higher capacitance compared to pure MXene and NFO, attributed to the

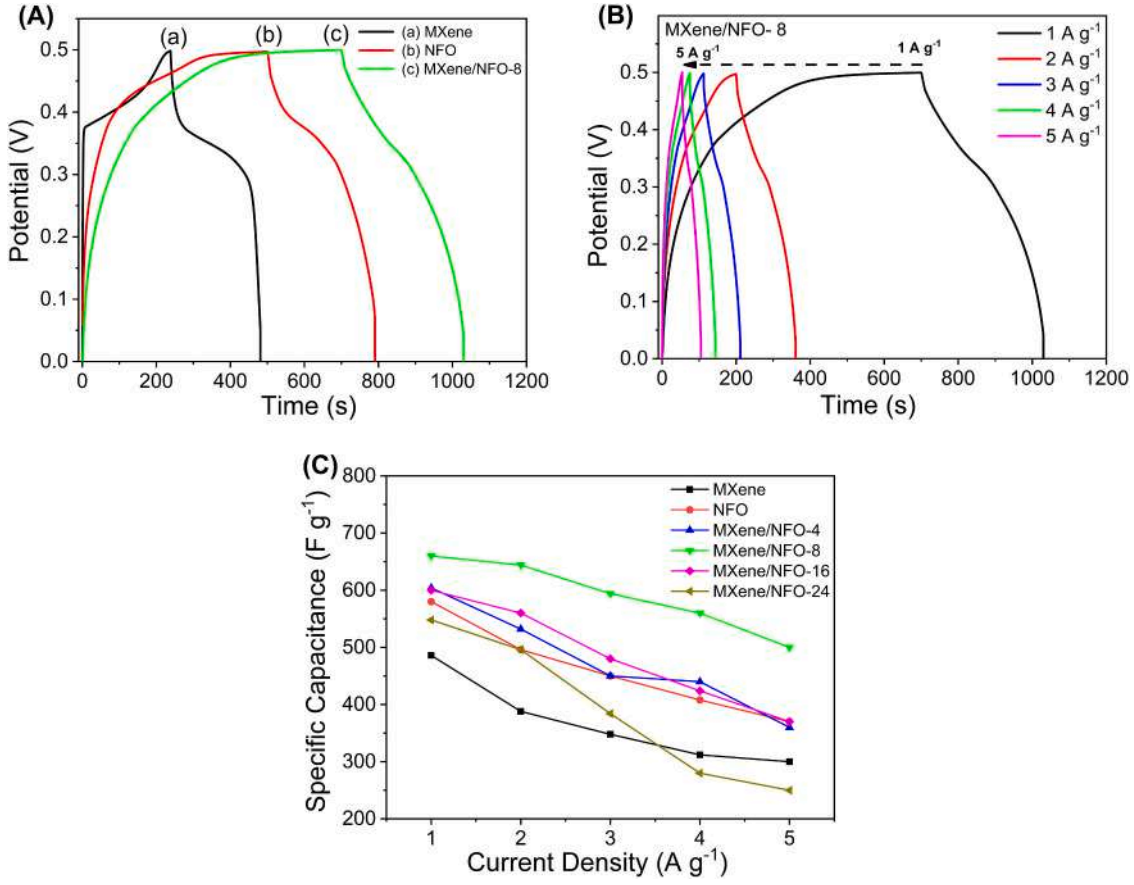

Fig. 8. (A) GCD curves of MXene (a), NFO (b), and MXene/NFO-8 (c) at 1 A g^{-1} current density. (B) GCD curves of MXene/NFO-8 across the current densities of 1, 2, 3, 4, and 5 A g^{-1}. (C) C_{SP} of MXene, NFO, and MXene/NFO-*x* electrodes at different current densities.

synergy between MOF-derived NFO and MXene. The NFO NPs act as spacers between MXene layers and play a crucial role in preventing the MXene layers from re-stacking [46]. The produced delaminated layers exhibit a larger surface area as seen from BET studies. The coexistence of the unique interlayer void space of MXene and the porous structure of NFO facilitates diffusion, thereby enhancing the overall pseudocapacitance. Furthermore, it was observed that the MXene/NFO-8 composite exhibits superior C_{SP} compared to the other investigated MXene/NFO-*x* composite electrodes. As the NFO content increases, the C_{SP} of the electrode initially rises due to the expansion of interlayer spacing in the composites along with the simultaneous rise in S_{BET}, allowing for more active sites for electrochemical reactions. [33]. Nevertheless, when the NFO content was further increased beyond 8 %, an excessive presence of NFO NPs may raise the internal resistance within the composite electrode. These aggregated NPs fill the pores within the MXene matrix causing a decline in C_{sp} [33].

Fig. 8B illustrates the GCD curves for MXene/NFO-8 while Fig. S5(B) and Fig. S5(C) show those for MXene and NFO at various current densities. As the current density increases, there is a reduction in discharge time suggesting that the electrolyte ions may readily pass through the electrode layers at a low current density, leading to a superior C_{SP} [47]. However, as current densities increase, the effectiveness of electrolyte ion interaction with the electrodes weakens, leading to a reduction in C_{SP}. The rate capability of MXene, NFO, and MXene/NFO-*x* at different current densities is depicted in Fig. 8C. It is worth mentioning that the MXene/NFO-8 can withstand high current density during charge and discharge. A comparative analysis of the performance of the MXene/NFO-8 composite with existing supercapacitor materials is presented in Table S2.

An EIS was conducted to further investigate the dynamics of electron transport and ion diffusion occurring at the electrode-electrolyte interface. The measurements were carried out in 100 kHz −0.01 Hz frequency range with 0.005 V/s amplitude. The resistances such as equivalent series (R_{ESR}) and charge transfer (R_{ct}) were evaluated using the Nyquist plots (Fig. 9A) along with an enlarged view shown in the inset. The Nyquist plot exhibits a critical point at the highest measured frequency, where the impedance intersects with the real axis (X-axis) corresponding to the R_{ESR} of the examined cell. The R_{ESR} represents the cumulative internal resistance within the cell originating from various cell components and electrolytes. R_{ESR} plays a pivotal role in dissipating stored energy and its magnitude limits the overall power performance and energy efficiency of the electrochemical cell. An arc in the high-frequency realm (R_{ct}) typically indicates the involvement of faradaic charge transfer resistance within the materials. The subsequent 45°-line region along the real axis of impedance represents the combined impact of both electrical double-layer (EDLC) and pseudocapacitance on the overall capacitance of the device. Table S3 illustrates the R_{ct} and R_s values for MXene, NFO, and MXene/NFO-*x*. It was observed that R_{ct} and R_s values for MXene/NFO-*x* composites were lower than the individual MXene and NFO electrodes. This suggests a rapid migration of both electrons and ions during the charge-discharge processes within the MXene/NFO-*x* composite, facilitated by the presence of the conducting network of MXene. MXene/NFO-8 exhibited a lower R_{ct} of 19.4 Ω/cm^2 and R_{ESR} of 0.6 Ω/cm^2, surpassing the performance of all other tested samples. Moreover, the experimental Nyquist data of the MXene/NFO-8 composite were analyzed by fitting it to Randel's equivalent electrical circuit model (Fig. S6). The derived values of R_{ct} and R_{ESR} values for MXene/NFO-8 from this equivalent circuit closely corroborate with the values obtained through experimental means.

Fig. 9B reveals a characteristic relationship between phase angle (Φ) and frequency in the Bode plot. In the Bode plot the phase angle reaches 45° at the "knee frequency" (f_0), where the impedance due to capacitance and resistance becomes equal. The relaxation time ($\tau_0 = f_0^{-1}$) which can be calculated from knee frequency, signifies the minimum duration needed for the device to dissipate all its stored energy efficiently, surpassing a 50 % efficiency threshold. The relaxation time constant τ_0 was found to be 57, 38, 49, and 161 ms for MXene/NFO-4, MXene/NFO-8, MXene/NFO-16, and MXene/NFO-24, respectively. MXene/NFO-8 exhibited superior frequency response due to shorter ionic transport pathways resulting in reduced internal resistance [48]. The radar plot shown in Fig. 10 summarizes the different matrices of supercapacitive performance of MXene/NFO-*x* composite electrodes.

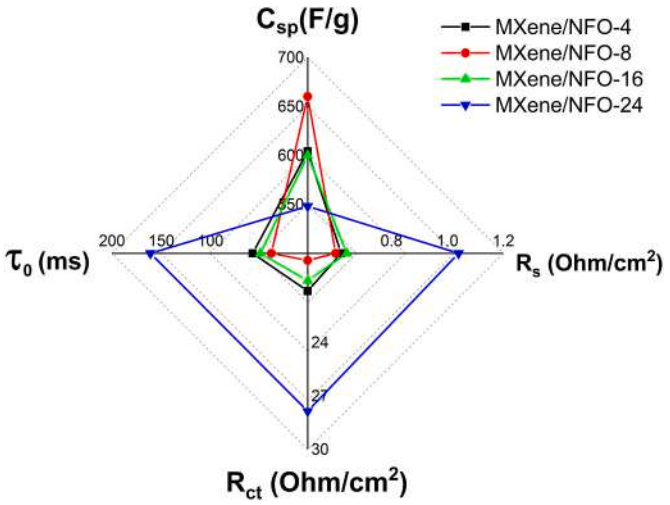

Fig. 10. Radar plot depicting metrices of supercapacitive performance of MXene/NFO-*x*.

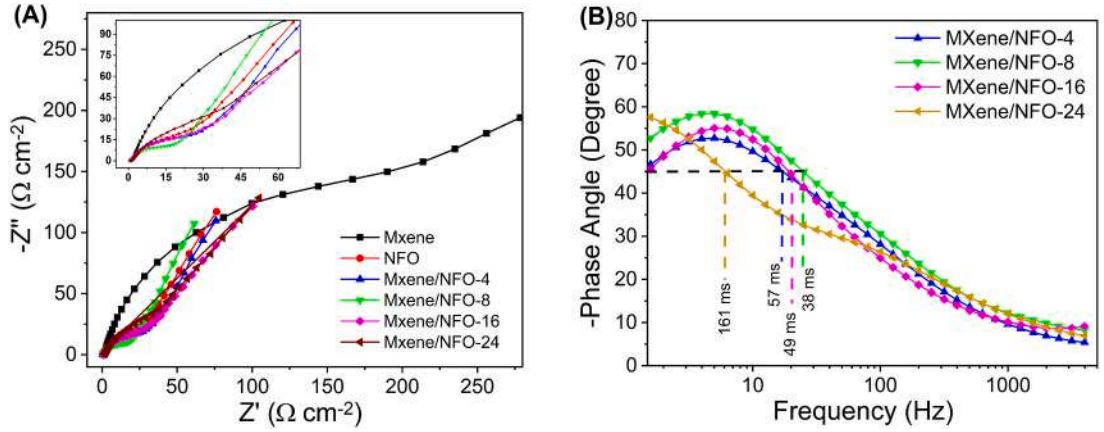

Fig. 9. (A) Nyquist plots of MXene, NFO, and MXene/NFO-*x*. The inset shows an enlarged view of Nyquist plots. (B) Bode plots of MXene/NFO-*x* composites.

3.2. MXene/NFO-8//AC asymmetric supercapacitor device

To evaluate the practicality of MXene/NFO-8 for supercapacitor application, an ASC device was designed with an all-solid-state configuration. The MXene/NFO-8//AC ASC device was constructed by using MXene/NFO-8 (positive electrode) and AC (negative electrode). To ensure accurate measurements for the ASC device using the two-electrode system, it is crucial to optimize both the voltage range and the mass ratio of positive and negative electrode materials. The mass ratio of MXene/NFO-8 to AC was determined as 0.49 through the charge equilibrium between positive and negative electrodes, as expressed by the following equation [49],

$$\frac{m^+}{m^-} = \frac{C_S - \Delta V^-}{C_S + \Delta V^+} \tag{10}$$

wherein C_s refers to the specific capacitance, m denotes the individual electrode mass, and ΔV signifies the potential difference during both the charging and discharging cycles for both the anode (+) and cathode (−).

As can be seen in Fig. 11A, the working potential window of AC is from −1.0 to 0 V and that of MXene/NFO-8 from 0 to 0.6 V. The CV profiles of the AC electrode exhibited a rectangle-like shape, typical of an EDLC type. To determine the most effective voltage window for the MXene/NFO-8//AC ASC device, the CV analysis was performed on the full cell, covering a voltage from 0 to 1.6 V at 50 mV s^{-1} scan rate (Fig. 11B). This ASC device has reached a steady potential of 1.45 V, after this the oxygen evolution reactions occur. Hence 0 to 1.45 V window was chosen for further measurements. The electrochemical characteristics of the MXene/NFO-8//AC ASC device were systematically evaluated using CVs across 10 to 100 mV s^{-1} scan rates (Fig. 11C). As the scan rate increased, all CV curves exhibited identical shapes, indicating the remarkable rate performance of the assembled ASC device. Fig. 11D shows the GCD profiles of the ASC device within a voltage range of 0–1.42 V. Good symmetry in the GCD curves suggests that MXene/NFO-8//AC ASC has outstanding capacitive characteristics. The C_{SP} of the MXene/NFO-8//AC was calculated from the corresponding GCD curves using Eq. (9) where m denotes the mass of the material deposited on both electrodes. The ASC could give the maximum C_{SP} of 62 F g^{-1} at 1 A g^{-1}. The E.D. and P.D. were determined using the succeeding equations,

$$\text{E.D.}\left(\text{Wh kg}^{-1}\right) = 0.5\,\frac{C_{SP}(V_2 - V_1)^2}{3.6} \tag{11}$$

$$\text{P.D.}\left(\text{W kg}^{-1}\right) = \frac{\text{E.D.}}{\Delta t}3600 \tag{12}$$

wherever C_{SP} indicates the specific capacitance of the ASC device, (V_2 – V_1) is the voltage window, and Δt refers to the discharge duration. The E.D. for the MXene/NFO-8//AC ASC device was found to be 17.36 W kg^{-1} at a P.D. of 718.48 Wh kg^{-1}. The comparison of the E.D. and P.D. of MXene/NFO-8//AC device with previously reported MXene-based supercapacitors is shown in a Ragone plot (Fig. 12A).

The electrochemical cyclic stability of the MXene/NFO-8//AC device was investigated over 5000 charge/discharge cycles at a 5 A g^{-1} current density (Fig. 12B). The inset of the figure shows the first and last few cycles revealing that GCD curves maintain their shape demonstrating the excellent cycling stability. The device shows retention of ~70 % of capacitance after 5000 cycles. Such long-term stability is attributed to the incorporation of NFO into the interlayers of MXene. The coulombic

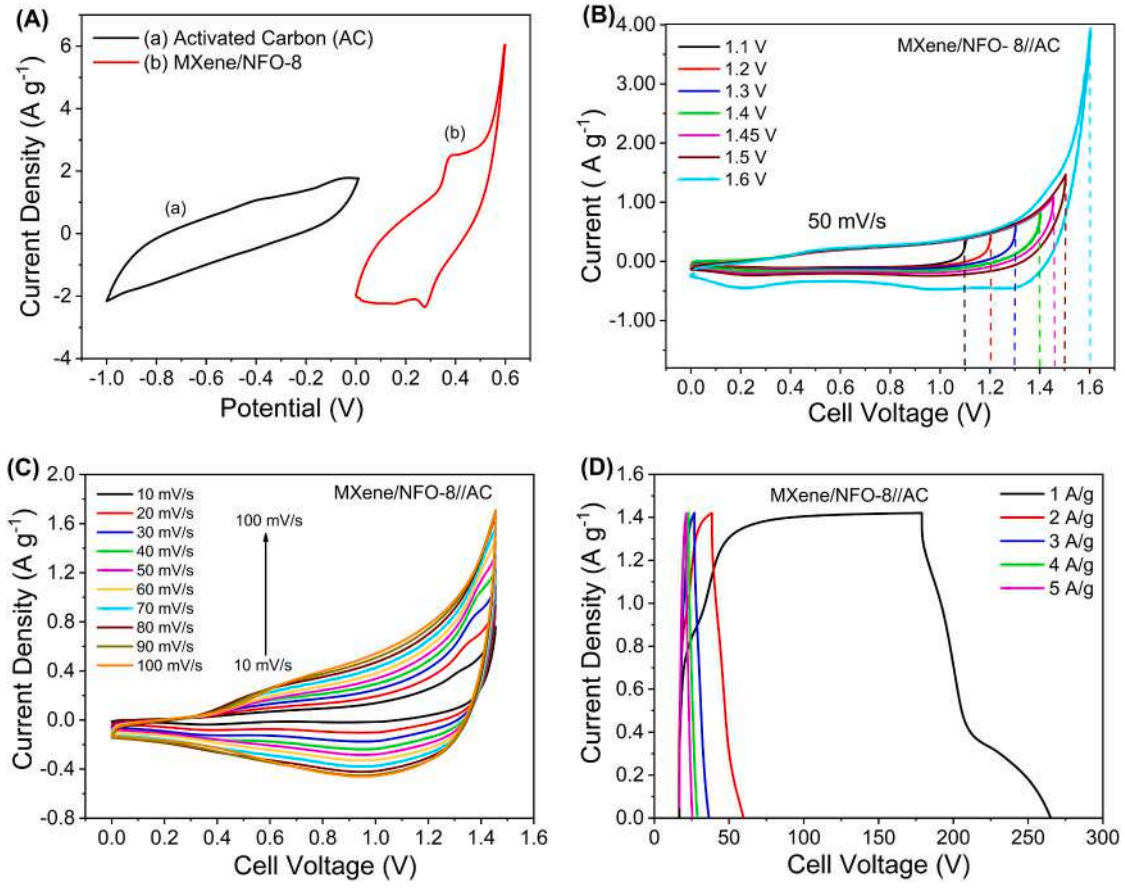

Fig. 11. (A) CV profiles of AC and MXene/NFO-8 at a scan rate of 50 mV s^{-1}. (B) CV curves of the MXene/NFO-8//AC ASC across various voltage windows. (C) CV curves of the MXene/NFO-8//AC ASC at 10 to 100 mV s^{-1} scan rate in voltage window 0 to 1.45 V. (D) GCD curves of the MXene/NFO-8//AC ASC across 0.5 1, 2, 3, 4, and 5 A g^{-1} current densities.

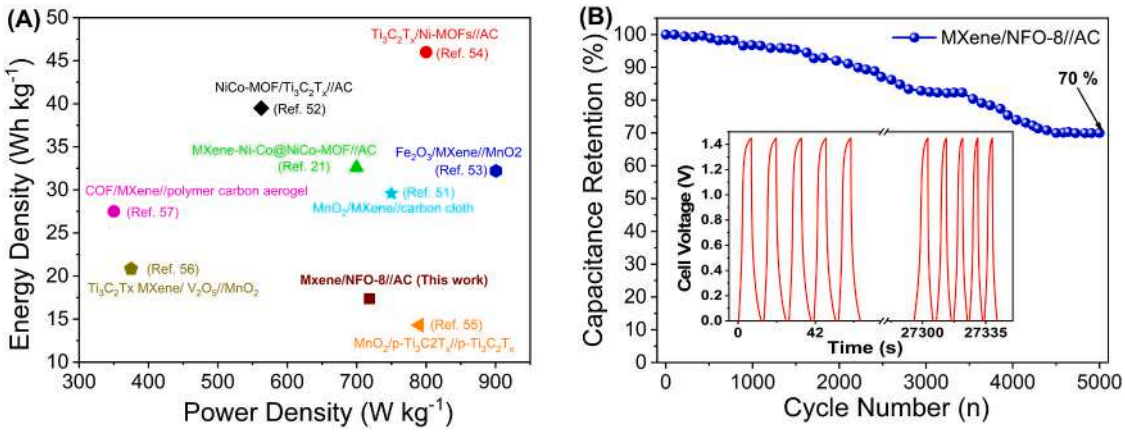

Fig. 12. (A) Ragone plot of MXene/NFO-8//AC device; The comparison of energy and power density with reported literature [21,51–57]. (B) GCD cyclic stability of MXene/NFO-8//AC at 5 A g^{-1} current density with inset showing first and last few GCD cycles.

efficiency of ~49 % was obtained for the MXene/NFO-8//AC device using the formula provided in the supplementary material file. NFO acts as a buffering region, absorbing and distributing the localized stresses during a volume expansion and contraction, thus preventing electrode disintegration [50]. To demonstrate the real application of the ASC device, two assembled MXene/NFO-8//AC ASC devices were serially connected, and charged for 60 s by a 3 V battery. The device can glow the red-light emitting diode (LED) for 70 s (Fig. S7).

4. Conclusions

We have successfully synthesized Ti_3C_2 MXene/NFO composites with different loading percentages of rhombohedral-shaped nickel ferrite nanoparticles (NFO NPs) for supercapacitor application. NFO NPs acted as spacers between the MXene layers which enhanced interlayer separation thereby facilitating effective charge transfer between the electrode and electrolyte. The MXene effectively synergized with NFO to deliver improved electrochemical performance. It was observed that a proper amount of NFO NPs is critical for enhancing the overall supercapacitive performance of the MXene/NFO film electrode. The MXene/NFO-8 electrode exhibited a C_{SP} of 660 F g^{-1} at the 1 A g^{-1}. An all-solid-state supercapacitor device MXene/NFO-8 //AC with PVA-HOH gel electrolyte demonstrated a high energy density of 17.36 Wh kg^{-1} at the power density of 718.48 W kg^{-1}. The device retained ~70 % of capacitance even after 5000 cycles.

CRediT authorship contribution statement

S.R. Shingte: Writing – original draft, Data curation. **V.D. Chavan:** Formal analysis. **R.P. Dhavale:** Formal analysis. **Deok-Kee Kim:** Visualization. **Hyung-Ho Park:** Visualization. **T.D. Dongale:** Writing – review & editing. **P.B. Patil:** Supervision, Conceptualization.

Declaration of competing interest

The authors declare that they have no known competing financial interests or personal relationships that could have appeared to influence the work reported in this paper.

Data availability

The data that has been used is confidential.

Acknowledgments

S.R. Shingte is thankful to the Chhatrapati Shahu Maharaj Research, Training, and Human Development Institute (SARTHI) for the fellowship. This work is supported by the Science and Engineering Research Board, Department of Science and Technology (DST-SERB), Government of India, for financial support through a grant (No. EMR/ 2017/ 001810). V.D. Chavan and Deok-Kee Kim acknowledge the financial support provided by the National Research Foundation of Korea (NRF), funded by the Ministry of Science and ICT (2016R1D1A1B01009537). R. P. Dhavale and H.H. Park would like to acknowledge that this work is supported by the National Research Foundation of Korea (NRF) grant funded by the Korean government (MSIT) (No. 2020R1A5A1019131).

Appendix A. Supplementary data

Supplementary data to this article can be found online at https://doi.org/10.1016/j.est.2024.112169.

References

[1] F. Barbir, T.N. Veziroğlu, H.J. Plass, Environmental damage due to fossil fuels use, Int. J. Hydrog. Energy 15 (1990) 739–749, https://doi.org/10.1016/0360-3199(90)90005-J.
[2] P. Vaghela, V. Pandey, A. Sircar, K. Yadav, N. Bist, R. Kumari, Energy storage techniques, applications, and recent trends: a sustainable solution for power storage, MRS Energy Sustain. 10 (2023) 261–276, https://doi.org/10.1557/S43581-023-00069-9/METRICS.
[3] A.G. Olabi, Q. Abbas, A. Al Makky, M.A. Abdelkareem, Supercapacitors as next generation energy storage devices: properties and applications, Energy 248 (2022) 123617, https://doi.org/10.1016/j.energy.2022.123617.
[4] Y. Shao, M.F. El-Kady, J. Sun, Y. Li, Q. Zhang, M. Zhu, H. Wang, B. Dunn, R. B. Kaner, Design and mechanisms of asymmetric supercapacitors, Chem. Rev. 118 (2018) 9233–9280, https://doi.org/10.1021/acs.chemrev.8b00252.
[5] S. Huang, X. Zhu, S. Sarkar, Y. Zhao, Challenges and opportunities for supercapacitors, APL Mater. 7 (2019) 1–14, https://doi.org/10.1063/1.5116146.
[6] B. Pal, S. Yang, S. Ramesh, V. Thangadurai, R. Jose, Electrolyte selection for supercapacitive devices: a critical review, Nanoscale Adv. 1 (2019) 3807–3835, https://doi.org/10.1039/c9na00374f.
[7] J.M. Lim, Y.S. Jang, H. Van, T. Nguyen, J.S. Kim, Y. Yoon, B.J. Park, D.H. Seo, K. K. Lee, Z. Han, K. Ostrikov, S.G. Doo, Advances in high-voltage supercapacitors for energy storage systems: materials and electrolyte tailoring to implementation, Nanoscale Adv. 5 (2023) 615–626, https://doi.org/10.1039/d2na00863g.
[8] J. Huang, Y. Xie, Y. You, J. Yuan, Q. Xu, H. Xie, Y. Chen, Rational design of electrode materials for advanced supercapacitors: from lab research to commercialization, Adv. Funct. Mater. 33 (2023) 2213095, https://doi.org/10.1002/ADFM.202213095.
[9] Y.A. Kumar, C.J. Raorane, H.H. Hegazy, T. Ramachandran, S.C. Kim, M. Moniruzzaman, 2D MXene-based supercapacitors: a promising path towards high-performance energy storage, J. Energy Storage 72 (2023) 108433, https://doi.org/10.1016/j.est.2023.108433.
[10] S. Wang, Y. Liu, Y. Liu, Z. Shi, J. Zhou, J. Zhu, W. Hu, Identifying the surface properties of $Ti_3C_2T_x$ MXene through transmission electron microscopy, Cell Rep. Phys. Sci. 3 (2022) 101151, https://doi.org/10.1016/j.xcrp.2022.101151.
[11] M. Alhabeb, K. Maleski, B. Anasori, P. Lelyukh, L. Clark, S. Sin, Y. Gogotsi, Guidelines for synthesis and processing of two-dimensional titanium carbide ($Ti_3C_2T_x$ MXene), Chem. Mater. 29 (2017) 7633–7644, https://doi.org/10.1021/acs.chemmater.7b02847.

[12] J. Li, X. Yuan, C. Lin, Y. Yang, L. Xu, X. Du, J. Xie, J. Lin, J. Sun, Achieving high pseudocapacitance of 2D titanium carbide (MXene) by cation intercalation and surface modification, Adv. Energy Mater. 7 (2017), https://doi.org/10.1002/aenm.201602725.

[13] Y. Wang, Y. Wang, Recent progress in MXene layers materials for supercapacitors: high-performance electrodes, SmartMat 4 (2023), https://doi.org/10.1002/smm2.1130.

[14] Y. Ma, Y. Yue, H. Zhang, F. Cheng, W. Zhao, J. Rao, S. Luo, J. Wang, X. Jiang, Z. Liu, N. Liu, Y. Gao, 3D Synergistical MXene/reduced graphene oxide aerogel for a piezoresistive sensor, ACS Nano 12 (2018) 3209–3216, https://doi.org/10.1021/acsnano.7b06909.

[15] Z. Ma, X. Zhou, W. Deng, D. Lei, Z. Liu, 3D porous MXene (Ti_3C_2)/reduced graphene oxide hybrid films for advanced lithium storage, ACS Appl. Mater. Interfaces 10 (2018) 3634–3643, https://doi.org/10.1021/acsami.7b17386.

[16] X. Xie, M.Q. Zhao, B. Anasori, K. Maleski, C.E. Ren, J. Li, B.W. Byles, E. Pomerantseva, G. Wang, Y. Gogotsi, Porous heterostructured MXene/carbon nanotube composite paper with high volumetric capacity for sodium-based energy storage devices, Nano Energy 26 (2016) 513–523, https://doi.org/10.1016/j.nanoen.2016.06.005.

[17] S. Dutt, A. Kumar, S. Singh, Synthesis of Metal Organic Frameworks (MOFs) and their derived materials for energy storage applications, Clean Technol. 5 (2023) 140–166, https://doi.org/10.3390/cleantechnol5010009.

[18] B. Pramanik, R. Sahoo, M.C. Das, pH-stable MOFs: design principles and applications, Coord. Chem. Rev. 493 (2023) 215301, https://doi.org/10.1016/j.ccr.2023.215301.

[19] S. Zheng, X. Li, B. Yan, Q. Hu, Y. Xu, X. Xiao, H. Xue, H. Pang, Transition-metal (Fe, Co, Ni) based metal-organic frameworks for electrochemical energy storage, Adv. Energy Mater. 7 (2017) 1–27, https://doi.org/10.1002/aenm.201602733.

[20] S. Zheng, H. Zhou, H. Xue, P. Braunstein, H. Pang, Pillared-layer Ni-MOF nanosheets anchored on Ti_3C_2 MXene for enhanced electrochemical energy storage, J. Colloid Interface Sci. 614 (2022) 130–137, https://doi.org/10.1016/J.JCIS.2022.01.094.

[21] J. Wang, J. Gong, H. Zhang, L. Lv, Y. Liu, Y. Dai, Construction of hexagonal nickel-cobalt oxide nanosheets on metal-organic frameworks based on MXene interlayer ion effect for hybrid supercapacitors, J. Alloys Compd. 870 (2021) 159466, https://doi.org/10.1016/J.JALLCOM.2021.159466.

[22] J. Liang, S. Li, F. Li, L. Zhang, Y. Jiang, H. Ma, K. Cheng, L. Qing, Defect engineering induces Mo-regulated Co_9Se_8/FeNiSe heterostructures with selenium vacancy for enhanced electrocatalytic overall water splitting in alkaline, J. Colloid Interface Sci. 655 (2024) 296–306, https://doi.org/10.1016/j.jcis.2023.11.010.

[23] B. Lu, S. Li, J. Pan, L. Zhang, J. Xin, Y. Chen, X. Tan, PH-controlled assembly of five new organophosphorus Strandberg-type cluster-based coordination polymers for enhanced electrochemical capacitor performance, Inorg. Chem. 59 (2020) 1702–1714, https://doi.org/10.1021/acs.inorgchem.9b02858.

[24] J. Yan, T. Liu, X. Liu, Y. Yan, Y. Huang, Metal-organic framework-based materials for flexible supercapacitor application, Coord. Chem. Rev. 452 (2022) 214300, https://doi.org/10.1016/j.ccr.2021.214300.

[25] P.D. Patil, S.R. Shingte, V.C. Karade, J.H. Kim, T.D. Dongale, S.H. Mujawar, A. M. Patil, P.B. Patil, Effect of annealing temperature on morphologies of metal organic framework derived $NiFe_2O_4$ for supercapacitor application, J. Energy Storage 40 (2021) 102821, https://doi.org/10.1016/j.est.2021.102821.

[26] T. Yu, S. Li, F. Li, L. Zhang, Y. Wang, J. Sun, In-situ synthesized and induced vertical growth of cobalt vanadium layered double hydroxide on few-layered V_2CT_x MXene for high energy density supercapacitors, J. Colloid Interface Sci. 661 (2024) 460–471, https://doi.org/10.1016/j.jcis.2024.01.206.

[27] T. Yu, S. Li, L. Zhang, F. Li, J. Wang, H. Pan, D. Zhang, In situ growth of ZIF-67-derived nickel-cobalt-manganese hydroxides on 2D V_2CT_x MXene for dual-functional orientation as high-performance asymmetric supercapacitor and electrochemical hydroquinone sensor, J. Colloid Interface Sci. 629 (2023) 546–558, https://doi.org/10.1016/j.jcis.2022.09.107.

[28] J. Li, D. Yan, S. Hou, Y. Li, T. Lu, Y. Yao, L. Pan, Improved sodium-ion storage performance of $Ti_3C_2T_X$ MXenes by sulfur doping, J. Mater. Chem. A 6 (2018) 1234–1243, https://doi.org/10.1039/c7ta08261d.

[29] I. Ayman, A. Rasheed, S. Ajmal, A. Rehman, A. Ali, I. Shakir, M.F. Warsi, $CoFe_2O_4$ nanoparticle-decorated 2D MXene: a novel hybrid material for supercapacitor applications, Energy Fuel 34 (2020) 7622–7630, https://doi.org/10.1021/acs.energyfuels.0c00959.

[30] X. Zhou, Y. Li, Q. Huang, Preparation of $Ti_3C_2T_x$/nizn ferrite hybrids with improved electromagnetic properties, Materials (Basel) 13 (2020), https://doi.org/10.3390/ma13040820.

[31] Z. Liu, J. Chen, M. Que, H. Zheng, L. Yang, H. Yuan, Y. Ma, Y. Li, X. Yang, 2D $Ti_3C_2T_x$ MXene/MOFs composites derived CoNi bimetallic nanoparticles for enhanced microwave absorption, Chem. Eng. J. 450 (2022) 138442, https://doi.org/10.1016/j.cej.2022.138442.

[32] W.K. Fan, A. Sherryna, M. Tahir, Advances in titanium carbide ($Ti_3C_2T_x$) MXenes and their Metal-Organic Framework (MOF)-based nanotextures for solar energy applications: a review, ACS Omega 7 (2022) 38158–38192, https://doi.org/10.1021/acsomega.2c05030.

[33] Y. Liu, Y. He, E. Vargun, T. Plachy, P. Saha, Q. Cheng, 3D porous Ti_3C_2 MXene/NiCo-MOF composites for enhanced lithium storage, Nanomaterials 10 (2020) 1–14, https://doi.org/10.3390/nano10040695.

[34] V. Biju, Ni 2p X-ray photoelectron spectroscopy study of nanostructured nickel oxide, Mater. Res. Bull. 42 (2007) 791–796, https://doi.org/10.1016/J.MATERRESBULL.2006.10.009.

[35] Q. Liu, Y., Y. He, E. Vargun, T. Plachy, P. Saha, Cheng, 3D porous Ti_3C_2 MXene/NiCo-MOF composites for enhanced lithium storage, Nanomaterials 10 (2017) 695.

[36] M. Thommes, K. Kaneko, A.V. Neimark, J.P. Olivier, F. Rodriguez-Reinoso, J. Rouquerol, K.S.W. Sing, Physisorption of gases, with special reference to the evaluation of surface area and pore size distribution (IUPAC Technical Report), Pure Appl. Chem. 87 (2015) 1051–1069, https://doi.org/10.1515/pac-2014-1117.

[37] D.K. Pattadar, H.N. Nambiar, S.L. Allen, J.B. Jasinski, F.P. Zamborini, Effect of metal nanoparticle aggregate structure on the thermodynamics of oxidative dissolution, Langmuir 37 (2021) 7320–7327, https://doi.org/10.1021/acs.langmuir.1c00565.

[38] R. Ramachandran, K. Rajavel, W. Xuan, D. Lin, F. Wang, Influence of Ti3C2Tx (MXene) intercalation pseudocapacitance on electrochemical performance of Co-MOF binder-free electrode, Ceram. Int. 44 (2018) 14425–14431, https://doi.org/10.1016/j.ceramint.2018.05.055.

[39] D. Du, R. Lan, K. Xie, H. Wang, S. Tao, Synthesis of $Li_2Ni_2(MoO_4)_3$ as a high-performance positive electrode for asymmetric supercapacitors, RSC Adv. 7 (2017) 13304–13311, https://doi.org/10.1039/c6ra28580e.

[40] J. Wang, J. Polleux, J. Lim, B. Dunn, Pseudocapacitive contributions to electrochemical energy storage in TiO_2 (anatase) nanoparticles, J. Phys. Chem. C 111 (2007) 14925–14931, https://doi.org/10.1021/jp074464w.

[41] T.S. Mathis, N. Kurra, X. Wang, D. Pinto, P. Simon, Y. Gogotsi, Energy storage data reporting in perspective—guidelines for interpreting the performance of electrochemical energy storage systems, Adv. Energy Mater. 9 (2019) 1–13, https://doi.org/10.1002/aenm.201902007.

[42] X. Feng, J. Ning, B. Wang, H. Guo, M. Xia, D. Wang, J. Zhang, Z.S. Wu, Y. Hao, Functional integrated electromagnetic interference shielding in flexible micro-supercapacitors by cation-intercalation typed $Ti_3C_2T_x$ MXene, Nano Energy 72 (2020) 104741, https://doi.org/10.1016/j.nanoen.2020.104741.

[43] A.M. Teli, S.A. Beknalkar, S.M. Mane, L.S. Chaudhary, D.S. Patil, S.A. Pawar, H. Efstathiadis, J.C. Shin, Facile hydrothermal deposition of Copper-Nickel sulfide nanostructures on nickel foam for enhanced electrochemical performance and kinetics of charge storage, Appl. Surf. Sci. 571 (2022) 151336, https://doi.org/10.1016/j.apsusc.2021.151336.

[44] S. Zheng, H. Zhou, H. Xue, P. Braunstein, H. Pang, Pillared-layer Ni-MOF nanosheets anchored on Ti_3C_2 MXene for enhanced electrochemical energy storage, J. Colloid Interface Sci. 614 (2022) 130–137, https://doi.org/10.1016/j.jcis.2022.01.094.

[45] S.M. Nikam, A. Sharma, M. Rahaman, A.M. Teli, S.H. Mujawar, D.R.T. Zahn, P. S. Patil, S.C. Sahoo, G. Salvan, P.B. Patil, Pulsed laser deposited $CoFe_2O_4$ thin films as supercapacitor electrodes, RSC Adv. 10 (2020) 19353–19359, https://doi.org/10.1039/d0ra02564j.

[46] R.C. Huan Liu, Xin Zhang, Yifan Zhu, Bin Cao, Qizhen Zhu, Peng Zhang, Xu Bin, Wu Feng, Electrostatic self-assembly of 0D–2D SnO_2 quantum dots/$Ti_3C_2T_x$ MXene hybrids as anode for lithium-ion batteries, Nano-Micro Lett. 11 (2019) 1–12.

[47] S. De, C.K. Maity, S. Acharya, S. Sahoo, J.J. Shim, G.C. Nayak, MXene (Ti3C2Tx) supported CoS_2/$CuCo_2S_4$ nanohybrid for highly stable asymmetric supercapacitor device, J. Energy Storage 50 (2022) 104617, https://doi.org/10.1016/j.est.2022.104617.

[48] T. Purkait, G. Singh, D. Kumar, M. Singh, R.S. Dey, High-performance flexible supercapacitors based on electrochemically tailored three-dimensional reduced graphene oxide networks, Sci. Rep. 8 (2018) 1–13, https://doi.org/10.1038/s41598-017-18593-3.

[49] L. Yue, S. Zhang, H. Zhao, Y. Feng, M. Wang, L. An, X. Zhang, One-pot synthesis $CoFe_2O_4$ / CNTs composite for asymmetric supercapacitor electrode, Solid State Ionics 329 (2019) 15–24.

[50] K.H. Oh, G.S. Gund, H.S. Park, Stabilizing $NiCo_2O_4$ hybrid architectures by reduced graphene oxide interlayers for improved cycling stability of hybrid supercapacitors, J. Mater. Chem. A 6 (2018) 22106–22114, https://doi.org/10.1039/C8TA04038A.

[51] H. Zhou, Y. Lu, F. Wu, L. Fang, H.J. Luo, Y.X. Zhang, M. Zhou, MnO_2 nanorods/MXene/CC composite electrode for flexible supercapacitors with enhanced electrochemical performance, J. Alloys Compd. 802 (2019) 259–268, https://doi.org/10.1016/J.JALLCOM.2019.06.173.

[52] Y. Wang, Y. Liu, C. Wang, H. Liu, J. Zhang, J. Lin, J. Fan, T. Ding, J.E. Ryu, Z. Guo, Significantly Enhanced Ultrathin NiCo-based MOF Nanosheet Electrodes Hybrided with $Ti_3C_2T_x$ MXene for High Performance Asymmetric Supercapacitors, 2020, pp. 50–59, https://doi.org/10.30919/es8d903.

[53] T. Shi, Y. Feng, T. Peng, B. Yuan, Sea Urchin-shaped Fe_2O_3 Coupled With 2D MXene Nanosheets as Negative Electrode for High-performance Asymmetric Supercapacitors vol. 381, 2021, pp. 1–7.

[54] X. Zhang, P. Mi, S. Yang, W. Lu, Y. Tian, M. Guo, N. Qu, Y. Zhao, MXenes Induced Formation of Ni-MOF Microbelts for High-performance Supercapacitors 592, 2021, pp. 1–6.

[55] X. Zhang, B. Shao, A. Guo, Z. Sun, J. Zhao, F. Cui, X. Yang, MnO 2 Nanoshells / Ti_3C_2 T_x MXene Hybrid Film as Supercapacitor Electrode 560, 2021, pp. 1–6.

[56] W. Luo, Y. Sun, Z. Lin, X. Li, Y. Han, J. Ding, T. Li, C. Hou, Y. Ma, Flexible $Ti_3C_2T_x$ MXene/V_2O_5 composite films for high-performance all-solid supercapacitors, J. Energy Storage 62 (2023) 106807, https://doi.org/10.1016/J.EST.2023.106807.

[57] N. An, Z. Guo, C. Guo, M. Wei, D. Sun, Y. He, W. Li, L. Zhou, Z. Hu, X. Dong, A novel COF / MXene film electrode with fast redox kinetics for high-performance flexible supercapacitor, Chem. Eng. J. 458 (2023) 1–7.